Desalination and Water Treatment
www.deswater.com
doi: 10.5004/dwt.2020.26282

204 (2020) 317–327
November

Adsorption molybdate ions using nanoscale zero valent iron-incorporated mesoporous carbons

Chen-Chia Huang*, Si-Hao Syu

Department of Chemical and Materials Engineering, National Yunlin University of Science and Technology, 123 University Road, Section 3, Douliu, Yunlin 64002, Taiwan, Tel./Fax: +886-5-534-2601; Ext. 4616/+886-5-531-2071; emails: huangchc@yuntech.edu.tw (C.-C. Huang), A0956168195@gmail.com (S.-H. Syu)

Received 5 February 2020; Accepted 19 June 2020

ABSTRACT

There were three methods for the preparation of iron nanoparticles incorporating ordered mesoporous carbons (OMCs): the incipient wetness impregnation technique (OMC-Fe(imp)), iron contained precursor (OMC-Fe) method, and citric acid chelated iron precursor (OMC-Fe-(citric)) method. The incorporated iron was reduced to nanoscale zero-valent iron (nZVI) by hydrogen at 673 K. The synthesized nZVI-incorporated OMCs were then used as an adsorbent to remove trace amount of molybdate ions from aqueous solutions. The texture characterization of OMCs was determined by nitrogen adsorption analysis. The morphology was observed by X-ray diffraction and transmission electron microscopy, and the surface functional groups were determined by X-ray photoelectron spectroscopy. The bulk iron contents were determined by thermal gravimetric analysis. The adsorption capacities of molybdate ions on the nZVI-incorporated OMCs were determined by using a batch reactor. Experimental results showed that the adsorption capacity of the OMC-Fe-(citric) is superior to that of OMC-Fe(imp) and OMC-Fe. At pH = 3 and initial concentration of 200 mg/L, the equilibrium adsorption capacities were 119 and 278 mg/g on OMC and OMC-Fe-(citric) containing 5 wt.% iron, respectively. The isotherm data and adsorption kinetics data were adequately fitted by the Langmuir equation and the pseudo-second-order adsorption kinetic model, respectively.

Keywords: Mesoporous carbon; Iron-incorporated; Molybdate ion; Adsorption; Nanoscale zero valent iron (nZVI)

1. Introduction

Molybdenum is classified as a trace metal, because it is not found free in nature on earth; it is found only in various oxidation states in minerals. About 86% of molybdenum produced is used in metallurgy, with the rest used in chemical applications. Most molybdenum compounds have low solubility in water, but when molybdenum contacts oxygen and water, the resulting molybdate ion is soluble. Molybdenum is one of the trace elements essential for living organisms and enters the human body through the food chain. If the cumulative concentration is too high, then it can cause many physiological hazards such as diarrhea, growth disorders, gout, infertility, and neonatal hypothermia, causing injury to lungs, liver, kidney, and other organs and even death [1]. National legislation states the discharge of molybdate ions in wastewater emission levels to be between 0.1 and 10 mg/L [2].

Wastewater containing molybdate ions can be treated in many ways, for example, filtration [3], flotation [4], ion exchange [5,6], and adsorption [7–20]. Adsorption has been proven to be an effective separation technique for

* Corresponding author.

1944-3994/1944-3986 © 2020 Desalination Publications. All rights reserved.

the treatment of low concentrations of metal ions [2–4]. The adsorption of molybdate ions is an effective and economical technique. There are different adsorbents used to remove molybdate ions from aqueous solution, such aspyrite [10], γ-Al_2O_3 [11], natrolite and clinoptolite-rich tuffs [12], sodium-saturated kaolinite [13], nano-ball allophone [14], titania goethite [15], carbon cloth [7–9], chitosan beads [16], ferric oxide gel [17], bentonite and powdered cockle shell [18], zeolite-supported magnetite [19], and activated carbon [1,20].

The zerovalent metal nanoparticle treatment technique has been proven to be effective at solving the most challenging environmental clearance problem, for example, chlorinated organic matter or heavy metal polluted soil and groundwater [21]. The nZVI has a high specific surface area and high surface activity and can be used to dispose of environmental pollutants, including chloro-carbon solvent [22], polychlorinated biphenyls [23], metal ions such as As(III), Pb(II), Cu(II), Ni(ii), Cr(VI), and so on [24,25]. However, there are still some challenges to practical application, such as easy aggregation of nZVI, high reactivity, and low stability. In order to prevent nZVI from forming a passivation layer and aggregation, recent studies used porous material to support nZVI [26–29]. However, the zerovalent iron granules that resulted from using the traditional wet dip method to deposit iron on a porous solid substrate surface are still large or aggregated. Huang et al. [30] reported removing molybdate from water using a hybridized zero-valent iron/magnetite/Fe(II) system.

Ordered mesoporous carbons (OMC) have been demonstrated as excellent catalytic supports due to their uniform and tunable pore size, regularly aligned pore architecture, high surface area, large pore volume, and thermal stability [31,32]. Several reports have shown that OMC can be synthesized through either a hard-templating approach [33,34] or soft-templating approach [35,36]. Tang et al. [37] recently used the co-dip method to feed ferric nitrate and sucrose into SBA-15, obtaining Fe/CMK-3 after high-temperature carbonization. The ferric nitrate resolved into ferric oxide (Fe_2O_3 and Fe_3O_4) in the high-temperature carbonization process, partially reducing to zerovalent iron; synergistic effect of absorption-coupled reduction hexavalent chromium was obtained, and then the removal efficiency of hexavalent chromium from an aqueous solution was increased. Sun et al. [38] proposed a chelate-assisted co-assembly route to synthesis high-quality ordered mesoporous carbons incorporated with highly dispersed uniform Fe_2O_3 nanoparticles for application in Fischer–Tropsch synthesis. They used soluble resol as a carbon source, iron nitrate as a metallic precursor, acetylacetone as a chelating agent, and Pluronic F127 as a template. The iron incorporated composite was further reduced by hydrogen at 673 K.

The references in the literature mostly used the traditional dip method or mixed porous material with iron powder and then reduced the iron to zerovalent iron. This study uses the pre-dip method, whereby the citric acid chelated iron is mixed into sucrose as a carbon source. The mesoporous silicon material SBA-15 as a template is made into mesoporous carbon with iron nanoparticles (OMC-Fe), and then the iron is reduced by high-temperature hydrogen to nZVI as an adsorbent to remove the slight amount of hexavalent Mo ions from the water. The OMC-Fe made by using different synthetic methods is compared with general OMC for the adsorption of Mo(VI) ion. The adsorption relation between adsorbent and Mo(VI) ion is discussed by isothermal adsorption pattern and adsorption kinetics pattern regressions. The OMC-Fe surface functional groups before and after adsorption are analyzed by XPS to discuss the adsorption mechanism.

2. Experimental

2.1. Materials

Triblock co-polymer (P123, $EO_{20}PO_{70}EO_{20}$, Mn:5,800), sucrose, and sodium molybdate dehydrate were all purchased from Aldrich. Tetraethyl orthosilicate (TEOS) and ferric nitrate 9-hydrate were purchased from Fluka and J.T. Baker, respectively. Citric acid monohydrate, nitric acid, sodium hydroxide, hydrochloric acid, and sodium sulfate were all purchased from Merck. All chemicals were analytical pure grade and were used as received. The solutions were prepared with high purity water (18.25 MΩ/cm) from a water purification system.

2.2. Preparation of nanoscale zero-valent iron-doped mesoporous carbon

2.2.1. Preparation of OMC

The SBA-15 silica template was prepared according to the process described in the literature [39,40]. OMC was synthesized under a nanocasting strategy as reported by Jun et al. [34]. Briefly, 1.25 g sucrose was dissolved into 5 mL aqueous solution containing 0.14 g H_2SO_4; 1.0 g SBA-15 was added and dispersed into the solution. The resulting mixture was heated in an oven at 373 K for 6 h and then at 433 K for another 6 h. Subsequently, 0.8 g of sucrose, 90 mg of sulfuric acid, and 5 mL pure water were again added to the pre-treated sample and the mixture was again subjected to the thermal treatment described above. The template-polymer composite was then pyrolyzed in a furnace under a nitrogen atmosphere up to 1,173 K under a heating rate of 5 K/min, holding the temperature for 6 h for carbonization. After cooling to room temperature, the mesoporous carbon was recovered after the dissolution of the silicon framework in 2 M NaOH solution, by filtration, washed several times with water and ethanol, and dried at 378 K.

2.2.2. Preparation OMC-Fe(imp)-X by the incipient wetness impregnation method

The weighed specific proportion of ferric nitrate was dissolved in the prepared 0.5 N HCl solution, mixed with acetone as a surfactant, and the OMC was put in an Erlenmeyer flask with ferric nitrate solution. After mixing, in order to make sure the OMC disperses in water uniformly, the mixture was vibrated by ultrasound for 1 h. Afterward, it was stirred at 100 rpm by a magnet at room temperature for 1 d. Finally, it was placed in 333 K oven for 2 d to remove most of the acetone. The code of the sample treated by a wet dip is OMC-Fe(imp)-X, where X is the designed iron content (*A* is 5 wt.%, *B* is 10 wt.%, and *C* is 15 wt.%).

2.2.3. Preparation of OMC-Fe-X by feeding sucrose with ferric nitrate

The proportioned ferric nitrate was dissolved in 5 g DI water, mixed well with a specific proportion of sucrose, and mixed with 0.14 g sulfuric acid; 1.0 g SBA-15 was then mixed with the prepared ferric solution uniformly. The subsequent process steps were identical to the OMC preparation. The code of the synthetic OMC-Fe sample is OMC-Fe-X, where X is the designed iron content.

2.2.4. Preparation of OMC-Fe(citric)-X by feeding sucrose with citric acid chelated-Fe

The proportioned ferric nitrate was dissolved in 5 g DI water and mixed with a specific proportion of citric acid to chelate Fe ion to form a citric acid chelated-Fe solution. The subsequent process steps were identical to the OMC preparation. The code of the synthetic OMC-Fe sample is OMC-Fe(citric)-X, where X is the designed iron content.

2.2.5. Reduction by hydrogen

The OMC-Fe was placed in the high-temperature furnace, supplied with nitrogen, and heated at 2 K/min to 673 K; the nitrogen was switched to hydrogen, the temperature was kept for 5 h, the iron ion was reduced to zerovalent iron, and the heating rate was low to avoid a fast reduction resulting in a sintering phenomenon. The hydrogen was then switched to nitrogen and cooled to room temperature. The sample code is OMC-Fe(citric)-X-R, where X represents the designed iron content, and R represents hydrogen reduction.

2.3. Characterization

Transmission electron microscopy (TEM) images were obtained on a JEOL JEM-2010 electron microscope (Tokyo, Japan) operated at 100 kV. X-ray diffraction (XRD) patterns were collected on a Miniflex II X-ray diffractometer equipped with CuKa radiation (k = 1.5406 A). The porous texture of the prepared OMC samples was characterized by physical adsorption of nitrogen at 77 K in a gas adsorption apparatus (Quantachrome Autosorb-1). Specific surface area (S_{BET}) was calculated using the Brunauer–Emmett–Teller (BET) equation at relative pressure between 0.005 and 0.3. The pore size was calculated using the Barrett–Joyner–Halenda (BJH) model in the range 1.4–200 nm and the density functional theory (DFT) method in the micropore range. The micropore volume was determined by the Dubinin–Radushkevich method. The surface elemental composition analyses were proposed based on the X-ray photoelectron spectroscopy (XPS, ULVAC-PHI, Kanagawa, Japan PHI 5000 VersaProbe/scanning ESCA microprobe) with a resolution of 0.5 eV. Thermogravimetric analysis (TGA) of the OMC samples was performed using thermal analysis instrument (model: TGA-2050), in order to evaluate the weight of iron-doped and thermal degradation of materials. Samples were heated to 1,073 K under an oxygen flow (40 mL/min), keeping a constant heating rate of 10 K/min and using a platinum crucible with a pinhole. The pH at the point of zero charges (pH_{pzc}) of the OMCs was measured by using the pH drift method. The pH of 0.01 M NaCl solution was adjusted to successive initial values between 2 and 8, by adding either HCl or NaOH. The OMCs (15 mg) were added in 15 mL of respective pH solution and left at room temperature for 48 h. After the pH stabilized, the final pH was measured. The graphs of pHs were drawn and used for the determination of points at which the initial and final pH values were equal [41].

2.4. Adsorption experiments

All batch adsorption experiments included sorption isotherm and sorption kinetics, and the effect of pH was performed in 250 mL glass conical flasks that underwent shaking at 100 rpm in a thermostatic shaker at 303 K. The pH values of the solutions were adjusted with 0.1 M HCl or 0.1 M NaOH using a pH meter. Sorption isotherms were studied by varying initial molybdate ions concentration from 25 to 200 mg/L. About 50 mg of OMCs were added into a 100 mL molybdate solution for each treatment unless otherwise stated. After finishing each experiment (24 h for isotherm studies), the adsorbents were separated, followed by an analysis of residual molybdenum concentration in the filtrate. Kinetic studies were carried out by taking samples at predetermined time intervals. The concentration of molybdenum ions in the supernatants was determined by an atomic absorption spectrometer (Perkin Elmer AAnalyst 400, Waltham, Massachusetts, U.S.). All the experiments were carried out in duplicate, and the average results were recorded. The isotherm capacity was calculated from the following mass balance relation:

$$q_e = \frac{\left(C_0 - C_e\right) \times V}{m} \tag{1}$$

where q_e (mg/g) is the equilibrium amount of Mo adsorbed per unit mass of adsorbent; C_0 (mg/L) and C_e (mg/L) are the initial Mo concentration and the equilibrium Mo concentration, respectively; and V (L) and m (g) are the test solution volume and mass of adsorbent, respectively.

For kinetic studies, the system volume decreases due to repeated sampling, and the adsorption capacity is calculated according to Eq. (2).

$$q_n = \frac{C_0 V_0 - C_n\left(V_0 - nv\right) - v\sum_1^n C_i}{m} \tag{2}$$

where q_n (mg/g) is accumulative adsorption capacity up to No. nth sampling; C_n (mg/L) is the concentration of No. nth sample solution; C_i (mg/L) is the concentration of No. ith sample solution; V_0 (L) is the initial solution volume; v (L) is the sample solution volume, and n is the number of times of sampling.

3. Results and discussion

3.1. Characterizations of adsorbents

Fig. 1 shows the transmission electron microscopy (TEM) images of the pristine OMC, OMC-Fe(imp)-B-R, OMC-Fe-B-R, and OMC-Fe(citric)-B-R. The TEM images in Fig. 1a indicates that the prepared OMC exhibits a highly

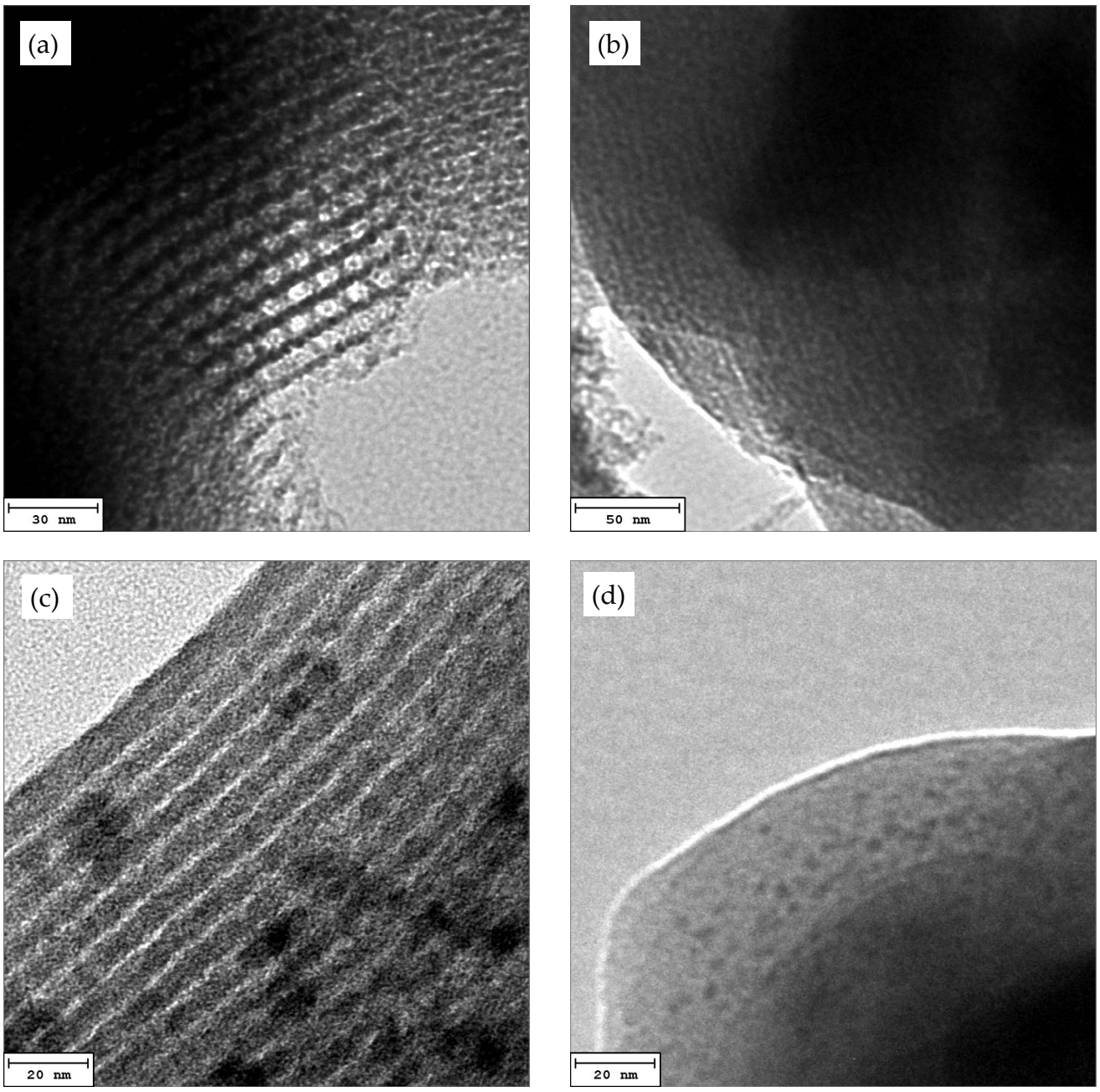

Fig. 1. TEM images of (a) OMC, (b) OMC-Fe(imp)-R, (c) OMC-Fe-B-R, and (d) OMC-Fe (citric)-B-R.

ordered mesoporous structure with linear arrays of mesopores. The pore diameters are around 10–12 nm. Fig. 1b for the OMC-Fe(imp)-B-R, which was prepared by the incipient wetness impregnation method, shows an obvious iron particle diameter of more than 50 nm, indicating that the iron particles in the carbonaceous material aggregate during the reduction process. Fig. 1c shows the TEM image of the OMC-Fe-B-R prepared by feeding sucrose with ferric nitrate and reduction with hydrogen. Iron particles are distinctly found in the carbon material. The particles are about 20 nm, which shows that agglomeration occurs. Fig. 1d is the TEM image of OMC-Fe(citric)-B-R prepared by citric acid chelated-Fe ions, reduced by thermal hydrogen in the process. It can be seen that uniform ferrite nanoparticles are highly dispersed in the carbon material and the particles are less than 8 nm.

Nitrogen adsorption/desorption isotherms at 77 K of the iron-doped OMCs after hydrogen reduction at 673 K are illustrated in Fig. 2a. The isotherms of all three iron-incorporated OMCs were found to type VI as defined by International Union of Pure and Applied Chemistry and exhibited a hysteresis loop with capillary condensation at a relative pressure that ranged between 0.5 and 0.95. From the shape and hysteresis of the isotherms, it is plausible to suggest that the OMCs show mesoporous structures. The pore size distributions of the iron-incorporated OMCs obtained using

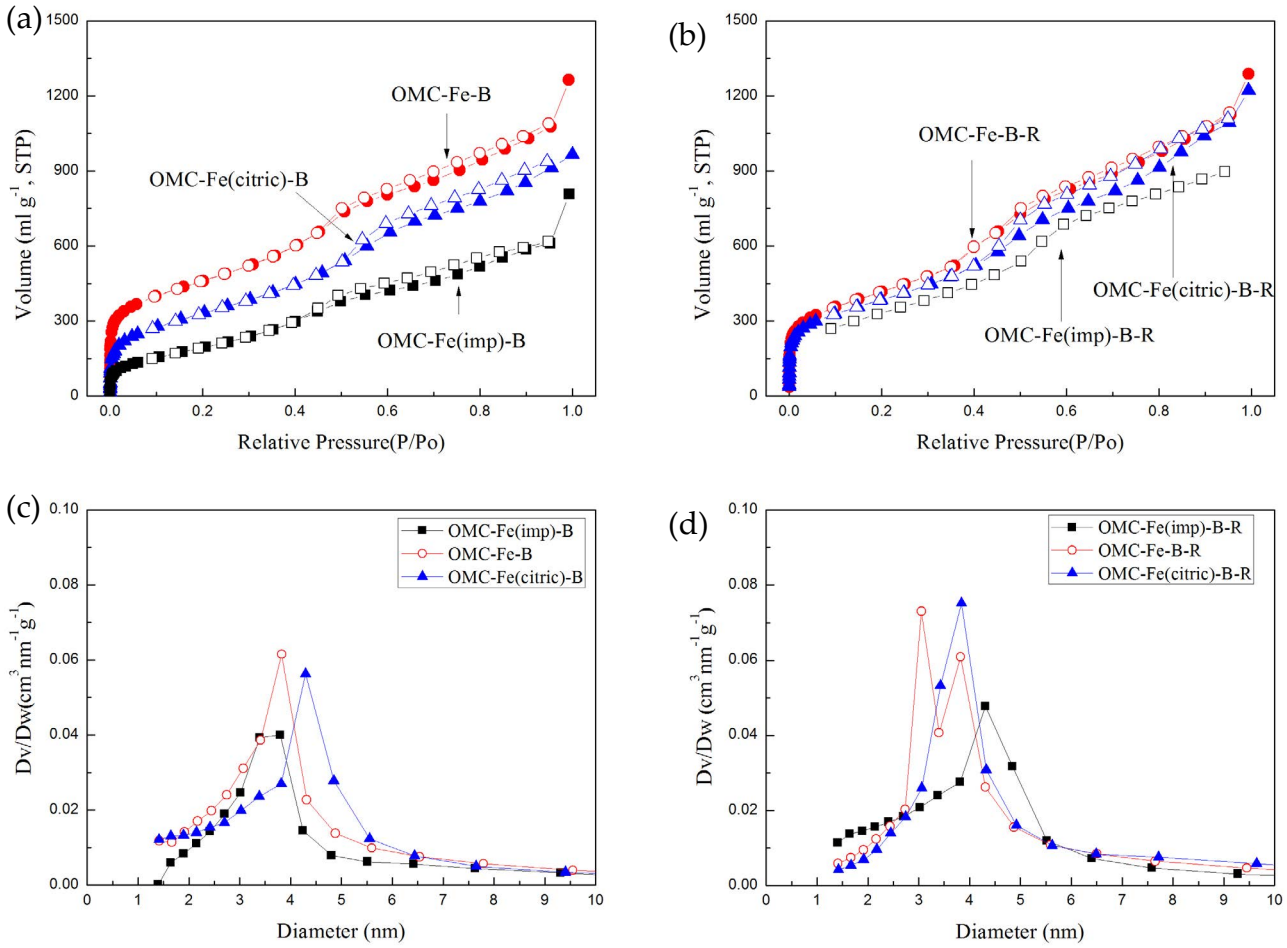

Fig. 2. N_2 adsorption–desorption isotherms at 77 K and the corresponding pore size distribution (determined by the BJH method) of iron-doped OMCs. Before (a and c) and after (b and d) hydrogen reduction at 673 K.

the Barrent–Joyner–Halenda (BJH) method and the DFT method are shown in Fig. 2b. The results clearly indicate that the OMC is nanoporous with quite a narrow pore-size distribution between 3 and 6 nm (mesopores). The total surface area S_{BET}, the total pore volume, and the micropore volumes of the OMC and the iron-incorporated OMC samples were calculated from nitrogen isotherm data and listed in Table 1. The BET specific surface area and total pore volume of the OMC are 1,410 m^2/g and 1.79 cm^3/g, respectively. Huang and Shen [42] reported the specific surface area and pore size of the CMK-3 were 1,075 m^2/g and 1.04 cm^3/g, respectively. The BET surface area and pore volume of the iron-incorporated OMCs by incipient wetness impregnation (OMC-Fe(imp)-B) dramatically decreased to less than 40% and 70% of those of the OMC, respectively. This result is due to pore blockage or partial pore filling by the presence of iron particles. The BET surface area and pore volume of the OMC-Fe-B are larger than those of the OMC.

During the high-temperature carbonization process, it is speculated that the reaction of ferric nitrate with sucrose causes defects in the carbonaceous material, resulting in an increase in the micropore volume. The specific surface area and total pore volume of OMC-Fe(cit) are slightly lower than those of the OMC, but the micropore volume is slightly higher than that of the OMC, which may be related to the decomposition of citric acid chelated-iron at high-temperature carbonization [38]. The BET specific surface area and pore volume of the iron-incorporated OMCs after hydrogen reduction at 673 K are also shown in Table 1. The specific surface area of OMC-Fe(imp)-B-R greatly increased, because the impregnated nitrate ions were decomposed at 673 K by hydrogen reduction. The released oxygen reacts with carbon to partially decompose the carbonaceous material. Both specific surface area and pore volume increased. The specific surface area and micropore volume of the OMC-Fe-B-R decreased slightly, but the mesopore volume increased slightly after reduction. The specific surface area of OMC-Fe(citric)-B-R increased, and both the micropore volume and mesopore volume also increased. It was found that OMC-Fe (citric)-B-R could obtain more favorable adsorption pore structures after hydrogen reduction at 673 K.

Fig. 3 shows TGA of the iron-incorporated OMCs in an oxygen atmosphere. As can be seen from Fig. 3, the main thermal degradation of the OMC occurs in the temperature range of 773–923 K under an oxygen atmosphere. Only about 4.59 wt.% remained, and the white ash residue was silicon, which could not be completely removed during the removal of the template. The thermogravimetric losses

Table 1
Texture characteristics of the OMCs

Sample	S_{BET} (m^2/g)	V_T (cm^3/g)	V_{meso} (cm^3/g)	V_{mic} (cm^3/g)
OMC	1,410	1.79	1.29	0.50
OMC-Fe(imp)-B	549	1.25	0.79	0.46
OMC-Fe-B	1,504	1.96	1.05	0.91
OMC-Fe(citric)-B	1,012	1.50	0.77	0.73
OMC-Fe(imp)-B-400	1,011	1.43	0.67	0.76
OMC-Fe-B-400	1,324	2.00	1.13	0.87
OMC-Fe(citric)-B-400	1,218	1.90	1.11	0.79

S_{BET}: BET specific surface area; V_T: total pore volume calculated from N_2 isotherm at $P/P_0 = 0.995$; V_{mic}: micropore volume was determined by the Dubinin–Radushkevithch equation; $V_{meso} = V_T - V_{mic.}$

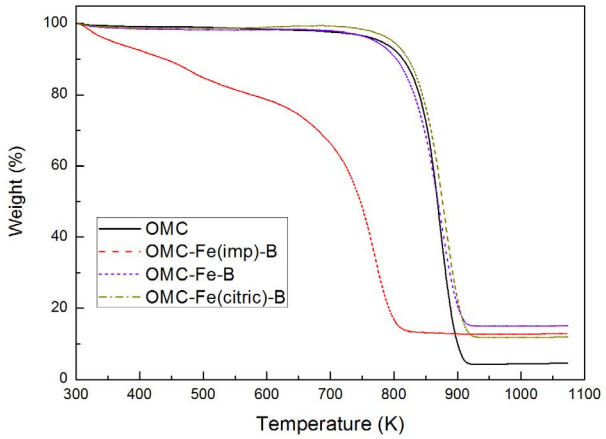

Fig. 3. Thermogravimetric diagrams of iron doped OMCs.

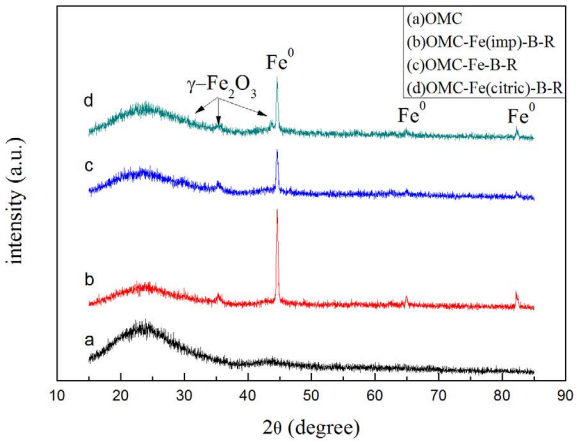

Fig. 4. XRD pattern of nZVI doped OMCs. (a) OMC, (b) OMC-Fe(imp)-B-R, (c) OMC-Fe-B-R, and (d) OMC-Fe(citric)-B-R.

of the OMC-Fe-B and the OMC-Fe(citric)-B are similar to that of the OMC, with 15.10 and 11.89 wt.% residual at 973 K, respectively. The residue was reddish-brown ash, presumed to be oxides of silicon and iron. After deducting Si, the iron contents of OMC-Fe-B and OMC-Fe(citric)-B were 7.36 and 5.11 wt.%, respectively. The TGA curve of the OMC-Fe(imp)-B, which was made by the traditional method of impregnation, is different from that of the other three samples. There is an initial weight loss after the start of heating. The weight loss below 573 K is about 20% and it can be attributed to the removal of physisorbed water and trapped acetone. Besides, the weight loss in the range of 673–823 K is about 58%, which is presumed that the impregnated nitrate ions and carbon reacted with each other to promote the gradual cleavage of carbon. At 823 K, 12.91 wt.% reddish-brown ash (silicon and iron oxide) remained, and after deducting silicon, 5.82wt.% of iron content was measured. The actual iron content of the three doped iron OMCs was slightly lower than the 10 wt.% designed at the time of preparation. Fig. 4 shows the XRD pattern of the iron-incorporated OMCs reduced by hydrogen at 673 K. It is obvious that the characteristic peaks of the graphitic framework of OMC are (002) and (101) diffraction peaks respectively at $2\theta = 23.0°$ and 44.0°. The iron-incorporated OMC reduced by hydrogen at 673 K has (101) characteristic peak, meaning there is still a good graphitic framework after reduction [43]. In addition, the iron-incorporated OMCs prepared by using three different methods and reduced by thermal hydrogen has the characteristic peaks of iron at 44.9°, 65.0°, and 82.0°. According to JCPDS, these peaks are the (110), (200), and (211) diffraction peaks of zero-valent iron, respectively, and the (220), (311), and (400) diffraction peaks of γ-Fe_2O_3 occur at 30.0°, 35.7°, and 43.0° [44].

3.2. Effect of solution pH

Fig. 5 shows the effect of different pH values on molybdate ion adsorption. The 100 mL 50 mg/L sodium molybdate solution and 25 mg adsorbent were mixed at a constant temperature of 303 K for 24 h. According to Fig. 5, the OMC has maximum adsorption capacity when the pH is 3, and the adsorption capacity decreases when the pH is lower or higher than 3. This can be attributed to the existence of molybdate ion at different pH values and the pH_{zcp} of the adsorbent. The pH_{zcp} values of the OMC, OMC-Fe-B, and OMC-Fe(citric)-B obtained by the pH drift method were 5.8, 5.5, and 5.7, respectively. The carbon material surface is positively charged when $pH < pH_{zcp}$. When the concentration is 50 mg/L, the molybdate ions are mostly $MoO_3(H_2O)$, $HMoO_4^-$, and MoO_4^{2-} when the pH is

3–5. MoO_4^{2-} is the dominant species from pH 5 to 12 [45]. The OH^- concentration in aqueous solution increases with pH, generating competitive adsorption with hexavalent molybdate anion, and thus the molybdate ion adsorption capacity decreases. Fig. 5 illustrates that the iron-incorporated OMC has maximum adsorption capacity for molybdate ion when the pH is 2. The adsorption capacity of molybdate ion on the iron-incorporated OMCs at pH 3 was similar to that at pH 2. In order to reduce the dosage of acid, pH = 3 was used as the adsorption operating condition.

3.3. Adsorption isotherm study

Figs. 6a and b show the adsorption isotherms of molybdate ions on the iron-incorporated OMCs before and after reduced by thermal hydrogen, respectively. The adsorption isotherms on the OMC are also presented in Fig. 6 for comparison. According to Fig. 6a, the OMC-Fe-B and OMC-Fe(citric)-B have higher adsorption capacity than the OMC, because the carbon material contains iron oxides, and the BET measurement results show that the micropore volume is larger than the OMC. The OMC-Fe-B has higher iron content and the largest micropore volume, and the experimental results show the maximum adsorption capacity for Mo(VI) acid ion. The iron oxide in the iron-incorporated OMC was reduced by hydrogen at 673 K to zero-valent iron. Fig. 6b presents that the adsorption capacity increases distinctly after reduction. The zero-valent iron is likely to be oxidized in general conditions, forming the ferriferous oxide. When the ferriferous oxide contacts water, the surface Fe–O–Fe bond performs hydroxylation and then forms a single water molecule film by hydrogen bonding with peripheral water molecules, known as hydration. The oxide surface is covered with OH^- [16], which is protonized in an acid environment to form positively charged Fe–OH_2^+, thus making it favorable for adsorbing the negatively charged molybdate ions. The γ-Fe_2O_3 peak was observed in the XRD pattern, and the γ-Fe_2O_3 forms X–OH_2^+ (X = Fe, C) in an acid environment, which is favorable for adsorbing the negatively charged molybdate ions. After the OMC-Fe prepared by using different methods is reduced by hydrogen at 673 K for 5 h, the OMC-Fe(citric)-B-R has the maximum adsorption capacity for molybdate ions, meaning the highly dispersed, and small-sized iron particles can enhance the adsorbability more effectively.

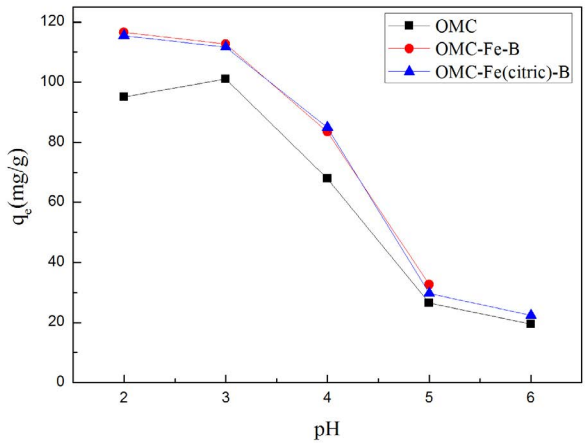

Fig. 5. Influence of initial pH value on the adsorption capacity of molybdate ions on iron-doped OMCs.

According to the aforesaid findings, the OMC-Fe(citric) prepared by using citric acid to disperse iron ions has small and uniformly dispersed iron particles and has the optimum adsorption capacity. Therefore, the iron content in OMC-Fe(citric) was changed in order to discuss the effect of iron content on adsorbing the molybdate ions from aqueous solution. Fig. 7 shows the adsorption isotherms of molybdate ions on the OMC-Fe(citric) with different iron contents after hydrogen reduction. The designed iron contents were 5, 10, and 15 wt.%, respectively, and the iron contents determined by TGA were 3.3, 5.1, and 8.6 wt.%, respectively. The adsorption test results show that the adsorption capacity decreases as the iron content in carbon material increases, perhaps because excessive iron blocks the channels and holes, and the higher the iron content in carbon material is, the more oxygen is released after high-temperature hydrogen reduction, and the more severely the carbon

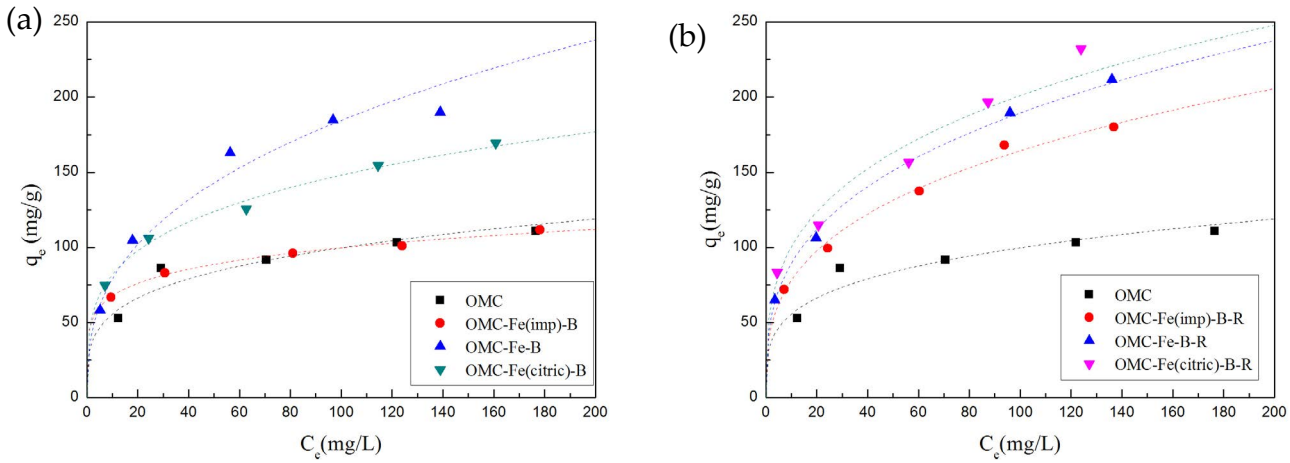

Fig. 6. Non-linear adsorption isotherms with the Freundlich model of molybdate ions adsorbed on iron-doped OMCs (a) before hydrogen reduction and (b) after hydrogen reduction at 673 K.

material structure is damaged. The specific surface area and micropore volume decrease distinctly as the iron content increases. Furthermore, excessive iron results in agglomeration, the iron has higher density than carbon, and the adsorbent weight increases with iron content, so that the adsorption capacity of adsorbent per unit mass for molybdate ions decreases. According to the BET measurement result, the OMC-Fe(citric)-A-R has larger micropore volume (1.21 cm^3/g) and small iron particles dispersed uniformly. Therefore, the OMC-Fe(citric)-A-R has the highest adsorption capacity for molybdate ions from aqueous solution.

In order to confirm the mechanism of the adsorption of molybdate ion by zero-valent nano iron-incorporated OMC, the chemical form of surface elements of OMC-Fe-(citric)-A-R after adsorbed molybdate ions was analyzed by XPS. Fig. 8a shows the full XPS spectra before and after adsorption of molybdate ions on the OMC-Fe(cit)-A-R. It is obvious that there is Mo 3d characteristic peak in spectrum 232–235 eV after adsorption. The inset of Fig. 8b shows the spectral pattern of Mo 3d of the OMC-Fe(cit)-A-R after adsorbed molybdate ions. The photoelectron peaks at 232.8 and 235.8 eV are for $Mo3d_{5/2}$ and $Mo3d_{3/2}$, respectively. This is similar to Barr [46], showing the presence of molybdenum on the adsorbent after adsorption. In addition, Fig. 8b shows the curve fitting bonding pattern of $Mo3d_{5/2}$, where the Mo(VI) is fitted only through bonding energy 235.8 eV [47]. The XPS shows that the valence state of Mo(VI) does not change when the OMC-Fe(citric)-A-R adsorbed molybdate ions from aqueous solution; the adsorption mechanism mainly by the attraction of the positively charged Fe–OH_2^+ to the negatively charged Mo(VI) acid ion in water. According to the BET measurement result, a small amount of iron incorporated in the OMC-Fe(citric)-A-R increases the specific surface area and micropore volume of carbon material, and the adsorption capacity of molybdate ions is enhanced effectively.

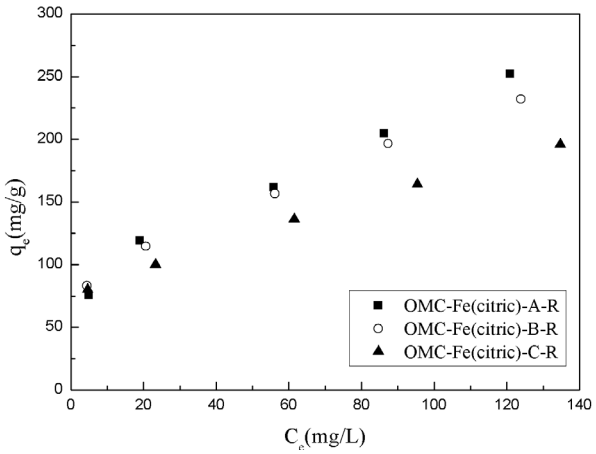

Fig. 7. Equilibrium adsorption isotherms of molybdate ions on different nZVI contents incorporated OMC-Fe(citric)-R. (A) 5 wt.%, (B) 10 wt.%, and (C) 15 wt.%.

The adsorption isotherm data were regressed by Langmuir and Freundlich isotherm equations, and the parameter values are listed in Table 2. The parameter q_e in Langmuir model is the coverage of monolayer molecules on the adsorbent surface. Table 2 shows that the q_e value after thermal hydrogen reduction is larger than that before reduction, perhaps because, after hydrogen reduction, the ferric oxide unfavorable for adsorption on the carbon material surface was reduced to zerovalent iron and γ-Fe_2O_3, which are favorable for adsorption. The zerovalent iron and γ-Fe_2O_3 form positively charged Fe–OH_2^+ in an acid environment, enhancing the driving force and adsorbability of carbon material to adsorb the negatively charged molybdate ions in solution, so that the adsorption capacity increases obviously. According to the q_e value of Langmuir isotherm in Table 2, the OMC equilibrium adsorption capacity is 119.0 mg/g; after 673 K hydrogen reduction, the equilibrium adsorption capacities of OMC-Fe(imp)-B-R, OMC-Fe-B-R, and OMC-Fe(citric)-B-R are 204.1, 232.6, and 256.4 mg/g, respectively. The adsorption performance is better after hydrogen reduction. The equilibrium adsorption capacity of the OMC-Fe(citric)-A-R is as high as 277.8 mg/g after 673 K hydrogen reduction, or higher than that of the OMC by 133%. In addition, according to the R^2 values in Table 2, both Langmuir and Freundlich models described adsorption isotherm data very well.

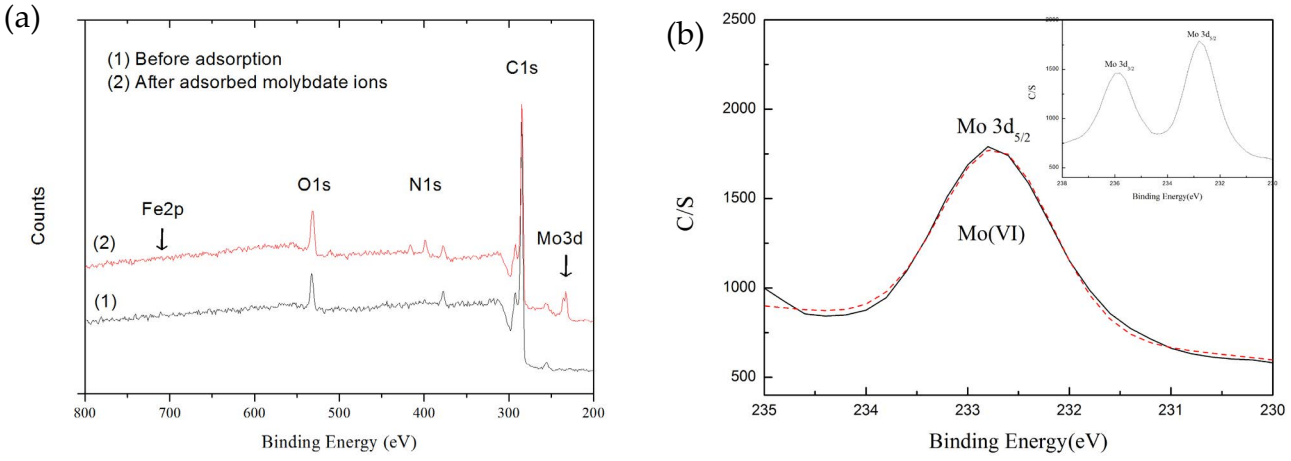

Fig. 8. (a) XPS survey of OMC-Fe(citric)-A-R before and after molybdenum ions adsorption and (b) XPS survey of Mo $3d_{5/2}$ of OMC-Fe(citric)-A-R adsorbed molybdate ions.

Table 2
Isotherm parameters for Mo(VI) adsorption on OMCs

	Langmuir			Freundlich		
	q_m (mg/g)	K_L (L/mg)	R^2	$1/n$	K_F (mg/g) (L/mg)$^{1/n}$	R^2
OMC	119.0	0.063	0.99	0.254	30.90	0.88
OMC-Fe(imp)-B	114.9	0.086	0.99	0.169	45.82	0.99
OMC-Fe-B	212.8	0.062	0.99	0.368	33.81	0.97
OMC-Fe(citric)-B	181.8	0.057	0.99	0.258	45.10	0.99
OMC-Fe(imp)-B-400	204.1	0.047	0.98	0.324	37.01	0.99
OMC-Fe-B-400	232.6	0.061	0.99	0.327	41.97	0.99
OMC-Fe(citric)-A-400	277.8	0.040	0.94	0.362	41.12	0.98
OMC-Fe(citric)-B-400	256.4	0.046	0.95	0.303	49.87	0.97
OMC-Fe(citric)-C-400	212.8	0.048	0.96	0.259	49.90	0.94

3.4. Adsorption kinetics

Fig. 9 shows the relationship between adsorption capacity and contact time under experimental conditions: initial concentration of 200 mg/L, pH 3, adsorbent 25 mg, and adsorption volume 100 mL. The iron contents in the OMC-Fe(imp)-A-R of traditional impregnation iron and the OMC-Fe(citric)-A-R of citric acid dispersed iron ions determined by TGA were 4.29 and 3.33 wt.%, respectively. The pseudo -first-order and pseudo-second-order adsorption kinetic models were used for fitting, and the parameters after fitting are compiled in Table 3. From Table 3, the k_1 values (the pseudo-first-order kinetic adsorption model) of OMC, OMC-Fe(imp)-A-R, and OMC-Fe(citric)-A-R are 0.2684, 0.1586, and 0.1274, respectively. The larger the k_1 value is, the faster is the adsorption reaction. The initial sorption constant h values (the pseudo-second-order kinetic adsorption model) of OMC, OMC-Fe(imp)-A-R, and OMC-Fe(citric)-A-R are 114.9, 555.6, and 357.1 mg/g/min, respectively. The larger the h value is, the faster is the initial adsorption reaction.

From Table 3, the OMC-Fe(imp)-A-R has higher initial adsorption rate constant, perhaps because there were huge particles agglomerated on the carbon material surface after thermal hydrogen reduction, and the surface iron particles can adsorb the molybdate ions in water rapidly. According to Table 3, the R^2 value of the pseudo-second-order adsorption kinetic model is higher than the pseudo-first-order adsorption kinetic model, and the q_e fitted by the pseudo-second-order adsorption kinetic model is close to the experimental value $q_{e,exp}$. Therefore, the pseudo-second-order adsorption kinetic model is more suitable to describe the adsorption kinetics.

3.5. Regeneration of used adsorbent

Regenerability of the adsorbent is one of key factors for practical application. The adsorption capacity of the fresh OMC-Fe(citric)-A-R (0.25 g/L) was 146.0 mg/g for adsorption 125 mg/L sodium molybdate solution (pH 3) at room temperature for 24 h. After adsorption, the OMC-Fe(citric)-A-R was desorbed by NaOH solution (pH 11.5) for 24 h, and reduced by hydrogen at 673 K for 5 h. The OMC-Fe(citric)-A-R adsorbs molybdate solution again at the same conditions. The second run adsorption capacity was 144.7 mg/g. The adsorption capacity loss is only 0.9%, meaning the OMC-Fe(citric)-A-R has good regenerability.

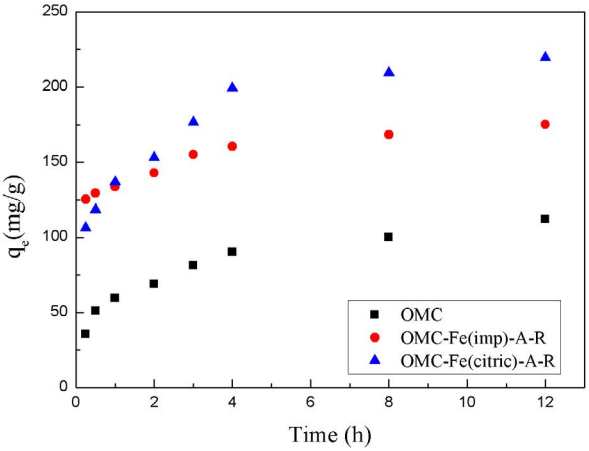

Fig. 9. Comparison of molybdate ions adsorption kinetics on various OMCs.

4. Conclusions

This study prepared three kinds of OMC-Fe, whereby according to a nitrogen adsorption/desorption experiment and the calculation of the BJH method, the mesopore size is 3–6 nm. The OMC-Fe was reduced by hydrogen at 673 K to nanoscale zerovalent iron. According to TEM, the nZVI is dispersed uniformly and small (<8 nm) in the chelate-assisted preparation OMC-Fe(citric)-B-R. The adsorption test results show that the OMC with nZVI can enhance the adsorption capacity of molybdate ions effectively after hydrogen reduction at 673 K. Adsorption capacity depends on specific surface area and micropore volume of the adsorbent, dispersion of nZVI particle, the size of nZVI, the content of nZVI, and the concentration of molybdate solution, pH, etc. The adsorption capacity decreases as the nZVI content increases. When the pH is 3, the molybdate ion concentration is 200 mg/L, the equilibrium adsorption

Table 3
Kinetic parameters for pseudo-first order and pseudo-second-order models

	Pseudo-first-order				Pseudo-second-order			
	$q_{e,exp}$ (mg/g)	q_e (mg/g)	k_1 (1/h)	R^2	q_e (mg/g)	k_2 (g/mg/h)	h (mg/g/h)	R^2
OMC	114.4	77.7	0.268	0.966	117.6	0.0087	114.9	0.992
OMC-Fe(imp)-A-400	184.0	55.0	0.159	0.967	178.6	0.0174	555.6	0.999
OMC-Fe(citric)-A-400	252.0	125.5	0.127	0.895	227.3	0.0069	357.1	0.997

capacity of the OMC-Fe(citric)-A-R is higher than the OMC by 133%. For the adsorption isotherms, the regression fit of the Freundlich isotherm model exhibits a better fitting. The pseudo-second-order adsorption kinetic model is more suitable for fitting adsorption kinetics data. The desorption regeneration test result shows that the OMC-Fe(citric)-A-R has good regenerability for adsorption of molybdate ions. The XPS spectra before and after adsorption of molybdate ions by iron-incorporated OMC were also compared. The adsorption mechanism was found to be an electrostatic attraction between the positively charged iron particles on the carbon material and the negatively charged molybdate ions. There is no chemical reaction found between Fe^0 and Mo(VI).

Acknowledgments

This work was financially supported by the Ministry of Science and Technology, R.O.C. under Grant no. MOST 103-2221-E-224-072.

References

[1] C. Namasivayam, D. Sangeetha, Removal of molybdate from water by adsorption onto $ZnCl_2$ activated coir pith carbon, Bioresource Technol., 97 (2006) 1194–1200.
[2] FWPCA, Report of the Committee on Water Quality Criteria, Federal Water Pollution Control Administration, U.S. Department of Interior, 1968.
[3] S.M. Yobilishetty, K.V. Marathe, Removal of molybdenum(VI) from effluent waste water streams by cross flow micellar enhanced ultrafiltration (MEUF) using anionic, non-ionic and mixed surfactants, Indian J. Chem. Technol., 21 (2014) 321–327.
[4] Y. Zhao, A.I. Zouboulis, K.A. Matis, Removal of molybdate and arsenate from aqueous solutions by flotation, Sep. Sci. Technol., 31 (1996) 769–785.
[5] S. Nishihama, K. Yoshizuka, Ion exchange adsorption of molybdenum with zeolitic adsorbent, J. Environ. Manage., 19 (2009) 365–369.
[6] M.M. El-Moselhy, A.K. Sengupta, R. Smith, Carminic acid modified anion exchanger for the removal and preconcentration of Mo(VI) from wastewater, J. Hazard. Mater., 185 (2011) 442–446.
[7] A. Afkhami, B.E. Conway, Investigation of removal of Cr(VI),Mo(VI), W(VI), V(IV), and V(V) oxy-ions from industrial waste-waters by adsorption and electrosorption at high-area carbon cloth, J. Colloid Interface Sci., 251 (2002) 248–255.
[8] A. Afkhami, T. Madrakian, A. Amini, Mo(VI) and W(VI) removal from water samples by acid treated high area carbon cloth, Desalination, 243 (2009) 258–264.
[9] A. Afkhami, T. Madrakian, Z. Karimi, The effect of acid treatment of carbon cloth on the adsorption of nitrite and nitrate ions, J. Hazard. Mater., 144 (2007) 427–431.
[10] B.C. Bostick, S. Fendorf, G.R. Helz, Differential adsorption of molybdate and tetrathiomolybdate on pyrite (FeS_2), Environ. Sci. Technol., 37 (2003) 285–291.
[11] C.H. Wu, C.Y. Kuo, C.F. Lin, S.L. Lo, Modeling competitive adsorption of molybdate, sulfate, selenate, and selenite using a Freundlich type multicomponent isotherm, Chemosphere, 47 (2002) 283–292.
[12] H. Faghihian, A. Malekpour, M.G. Maragheh, Adsorption of molybdate ion by natrolite and clinoptilolite-rich tuffs, Int. J. Environ. Pollut., 18 (2002) 181–189.
[13] P. J. Phelan, S.V. Mattigod, Adsorption of molybdate anion (MoO_4^{2-}) by sodium-saturated kaolinite, Clays Clay Miner., 32 (1984) 45–48.
[14] E.A. Elhadi, N. Matsue, T. Henmi, Effect of molybdate adsorption on some surface properties of nano-ball allophane, Clay Sci., 11 (2001) 405–416.
[15] P. Zhang, D.L. Sparks, Kinetics and mechanisms of molybdate adsorption/desorption at the goethite/water interface using pressure-jump relaxation, Soil Sci. Soc. Am. J., 53 (1989) 1028–1034.
[16] E. Guibal, C. Milot, J.M. Tobin, Metal-anion sorption by chitosan beads: equilibrium and kinetic studies, Ind. Eng. Chem. Res., 37 (1998) 1454–1463.
[17] J.C. Ryden, J.K. Syers, R.W. Tillman, Inorganic anion sorption and interactions with phosphate sorption by hydrous ferric oxide gel, Eur. J. Soil Sci., 38 (1987) 211–217.
[18] A. Mojiri, Z. Ahmad, R.M. Tajuddin, M.F. Arshad, V. Barrera, Molybdenum(VI) removal from aqueous solutions using bentonite and powdered cockle shell; optimization by response surface methodology, Global NEST J., 19 (2017) 232–240.
[19] B. Verbinnen, C. Block, D. Hannes, P. Lievens, M. Vaclavikova, K. Stefusova, G. Gallios, C. Vandecasteele, Removal of molybdate anions from water by adsorption on zeolite-supported magnetite, Water Environ. Res., 84 (2012) 753–760.
[20] S.L.C. Ferreira, H.M.C. Andrade, H.C. doe Santos, Characterization and determination of the thermodynamic and kinetic properties of the adsorption of the molybdenum(VI)-calmagite complex onto active carbon, J. Colloid Interface Sci., 270 (2004) 276–280.
[21] W.-X. Zhang, Nanoscale iron particles for environmental remediation: an overview, J. Nanopart. Res., 5 (2003) 323–332.
[22] C. Wang, W. Zhang, Synthesizing nanoscale iron particles for rapid and complete dechlorination of TCE and PCBs, Environ. Sci. Technol., 31 (1997) 2154–2156.
[23] J. Xu, A. Dozier, D. Bhattacharyya, Synthesis of nanoscale bimetallic particles in polyelectrolyte membrane matrix for reductive transformation of halogenated organic compounds, J. Nanopart. Res., 7 (2005) 449–467.
[24] M.J. Alowitz, M.M. Scherer, Kinetics of nitrate, nitrite, and Cr(VI) reduction by iron metal, Environ. Sci. Technol., 36 (2002) 299–306.
[25] S.R. Kanel, B. Manning, L. Charlet, H. Choi, Removal of arsenic(III) from groundwater by nanoscale zero-valent iron, Environ. Sci. Technol., 39 (2005) 1291–1298.
[26] Y. Zhang, Y. Li, J. Li, G. Sheng, Y. Zhang, X. Zheng, Enhanced Cr(VI) removal by using the mixture of pillared bentonite and zero-valent iron, Chem. Eng. J., 185 (2012) 243–249.
[27] L. Shi, X. Zhang, Z. Chen, Removal of chromium(VI) from wastewater using bentonite-supported nanoscale zero-valent iron, Water Res., 45 (2011) 886–892.
[28] T. Liu, L. Zhao, D. Sun, X. Tan, Entrapment of nanoscale zero-valent iron in chitosan beads for hexavalent chromium removal from wastewater, J. Hazard. Mater., 184 (2010) 724–730.

[29] X. Lv, J. Xu, G. Jiang, X. Xu, Removal of chromium(VI) from wastewater by nanoscale zero-valent iron particles supported on multiwalled carbon nanotubes, Chemosphere, 85 (2011) 1204–1209.
[30] Y.H. Huang, C. Tang, H. Zeng, Removing molybdate from water using a hybridized zero-valent iron/magnetite/Fe(II) treatment system, Chem. Eng. J., 200 (2012) 257–263.
[31] R. Ryoo, S.H. Joo, M. Kruk, M. Jaroniec, Ordered mesoporous carbons, Adv. Mater., 13 (2001) 677–681.
[32] A. Eftekhari, Z. Fan, Ordered mesoporous carbon and its applications for electrochemical energy storage and conversion, Mater. Chem. Front., 1 (2017) 1001–1027.
[33] D. Zhao, Q. Huo, J. Feng, B.F Chmelka, G.D. Stucky, Nonionic triblock and star diblock copolymer and oligomeric surfactant syntheses of highly ordered, hydrothermally stable, mesoporous silica structures, J. Am. Chem. Soc., 120 (1998) 6024–6036.
[34] S. Jun, S.H. Joo, R. Ryoo, M. Kruk, M. Jaroniec, Z. Liu, T. Ohsuna, O. Terasaki, Synthesis of new, nanoporous carbon with hexagonally ordered mesostructure, J. Am. Chem. Soc., 122 (2000) 10712–10713.
[35] X. Wang, C. Liang, S. Dai, Facile synthesis of ordered mesoporous carbons with high thermal stability by self-assembly of resorcinol-formaldehyde and block copolymers under highly acidic conditions, Langmuir, 24 (2008) 7500–7505.
[36] J. Jin, N. Nishiyama, Y. Egashira, K. Ueyama, Pore structure and pore size controls of ordered mesoporous carbons prepared from resorcinol/formaldehyde/triblock polymers, Microporous Mesoporous Mater., 118 (2009) 218–223.
[37] L. Tang, G.-D. Yang, G.-M. Zeng, Y. Cai, S.-S. Li, Y.-Y. Zhou, Y. Pang, Y.-Y. Liu, Y. Zhang, B. Luna, Synergistic effect of iron doped ordered mesoporous carbon on adsorption-coupled reduction of hexavalent chromium and the relative mechanism study, Chem. Eng. J., 239 (2014) 114–122.
[38] Z. Sun, B. Sun, M. Qiao, J. Wei, Q. Yue, C. Wang, Y. Deng, S. Kaliaguine, D. Zhao, A general chelate-assisted co-assembly to metallic nanoparticles-incorporated ordered mesoporous carbon catalysts for Fischer–Tropsch synthesis, J. Am. Chem. Soc., 134 (2012) 17653–17660.
[39] M.J. Lázaro, L. Calvillo, E.G. Bordejé, R. Moliner, R. Juan, C.R. Ruiz, Functionalization of ordered mesoporous carbons synthesized with SBA-15 silica as template, Microporous Mesoporous Mater., 103 (2007) 158–165.
[40] M. Kruk, M. Jaroniec, C.H. Ko, R. Ryoo, Characterization of the porous structure of SBA-15, Chem. Mater., 12 (2000) 1961–1968.
[41] G. Newcombe, R. Hayes, M. Drikas, Granular activated carbon: importance of surface properties in the adsorption of naturally occurring organics, Colloids Surf., A, 78 (1993) 65–71.
[42] C.-C. Huang, S.-H. Shen, Adsorption of CO_2 on chitosan modified CMK-3 at ambient temperature, J. Taiwan Inst. Chem. Eng., 44 (2013) 89–94.
[43] T.W. Kim, I.S. Park, R. Ryoo, A synthetic route to ordered mesoporous carbon materials with graphitic pore walls, Angew. Chem., 42 (2003) 4375–4379.
[44] M. Baikousi, A.B. Bourlinos, A. Douvali, T. Bakas, D.F. Anagnostopoulos, J. Tuček, K. Šafářová, R. Zboril, M.A. Karakassides, Synthesis and characterization of γ-Fe_2O_3/carbon hybrids and their application in removal of hexavalent chromium ions from aqueous solutions, Langmuir, 28 (2012) 3918–3930.
[45] D. Qian, Y. Su, Y. Huang, H. Chu, X. Zhou, Y. Zhang, Simultaneous molybdate (Mo(VI)) recovery and hazardous ions immobilization via nanoscale zerovalent iron, J. Hazard. Mater., 344 (2018) 698–706.
[46] T.L. Barr, An ESCA study of the termination of the passivation of elemental metals, J. Phys. Chem., 82 (1978) 1801–1810.
[47] G.T. Kim, T.K. Park, H. Chung, Y.T. Kim, M.H. Kwon, J.G. Choi, Growth and characterization of chloronitroaniline crystals for optical parametric oscillators: I. XPS study of Mo-based compounds, Appl. Surf. Sci., 152 (1999) 35–43.